RESEARCH ARTICLE

Journal
American Ceramic Society

Complete control and strengthening over iron oxide porous structures freeze cast under oscillating magnetic fields

Josh R. Fernquist [ORCID] | **Steven E. Naleway**

Department of Mechanical Engineering, University of Utah, Salt Lake City, Utah, USA

Correspondence
Josh R. Fernquist, Department of Mechanical Engineering, University of Utah, Salt Lake City, UT, USA.
Email: josh.fernquist@utah.edu, jrfernquist812@gmail.com

Abstract

Porous scaffolds can be utilized in a variety of biomedical as well as mechanical applications. The process of freeze casting is a successful method to fabricate these porous structures but with ideal characteristics in only one direction (the ice-growth direction). The application of magnetic fields led to an increase in both the microstructural control and mechanical strength in an additional orthogonal direction. The application of these weak, uniform fields (≤ 20 mT), in particular oscillating fields from a Helmholtz coils setup, has led to increases in mechanical strength through microstructural alignment in multiple material types. However, structures fabricated from these uniform fields have primarily been compared to each other, with little research comparing them to structures fabricated under strong, non-uniform fields from permanent magnet setups. Therefore, iron-oxide scaffolds were fabricated under weak, uniform fields (≤ 20 mT) as well as strong, non-uniform fields (≥ 20 mT), and their mechanical and microstructural properties were compared to one another. The application of weak, uniform fields led to superior mechanical properties compared to those produced from the application of strong, non-uniform fields, no distortions in the physical structure of the freeze-cast scaffold, and the best microstructural alignment ever seen in freeze-cast structures.

KEYWORDS
electromagnets, freeze casting, Helmholtz coils, magnetics, oscillating magnetic field, uniform magnetic field

1 | INTRODUCTION

Tailored porous scaffolds are structures that can be utilized in a variety of biomedical as well as mechanical applications, such as filters,[1] bone implants,[2–5] biomedical scaffolds,[6,7] or capacitors.[8] Freeze casting is a fabrication technique to create these tailored porous structures successfully and repeatedly.[9–11] The typical freeze-casting process consists of the following:

1. Mixing a slurry that consists of one or multiple solid loading compounds, a freezing agent, one or multiple polymeric binders, and additional additives such as particle dispersants.
2. Directionally freezing the slurry, generally by pouring the mixed slurry into a mold atop a cold finger submerged in a cold bath. This causes the freezing agent to directionally solidify and template the structure.

3. Placing the solidified structure into a freeze dryer to sublimate the crystals formed by the freezing agent, resulting in a porous green body.
4. Densifying the green body (e.g., through sintering in a furnace). This leads to a dense porous scaffold, templated by the freezing agent crystals.

During the freeze-casting process, there are several factors that can control both the structure and properties of the resultant freeze-cast structure. This includes both intrinsic and extrinsic factors. An intrinsic factor is one that is changed internally during the process, such as adding additional slurry additives,[10,12–15] or changing the freezing rates.[16–18] An extrinsic factor is one that is applied externally during the freeze-casting process, such as altering the freezing direction[19–25] or the application of external forces (e.g., electric, acoustic, magnetic).[14,25–31] When looking at these extrinsic factors, the application of external forces, specifically magnetic fields, has been shown to dynamically control the mechanical properties of freeze-cast structures at user-specified locations.[14,27,30–32]

These externally applied magnetic fields have been of particular interest in recent freeze-casting research as the freeze-casting process tends to produce structures that are mechanically strong in the ice-templating direction but weak in the other two orthogonal directions.[14,27] Through applying these magnetic fields transverse to the ice-templating direction, it has been shown to lead to increases in mechanical strength in said transverse direction, with up to 200% increases in compressive strength.[30,31] In all cases, the magnetic field was applied during the freezing process (step 2 above), as this is when the particles, which would be suspended in the freezing agent, are most susceptible to the magnetic field.[31–33] Most of these studies utilized permanent magnet setups to apply these magnetic fields during the freeze-casting process.[14,27,29,34] While these permanent magnet setups allow for fields of very large magnitudes (e.g., >75 mT), this is done at the cost of creating a large magnetic field gradient across the freeze-cast structure.[29] This gradient is caused by the field strength being significantly greater near the permanent magnets than at the center of the setup.[29] The consequence of this field gradient is the migration of the magnetically susceptible particles to the surfaces closest to the permanent magnet, thus causing particle agglomeration and distortion of the freeze-cast structure.[34] This particle agglomeration leads to an inhomogeneity of the material density and strength.

To combat this inhomogeneity of material strength, recent research has shown the ability to control freeze-cast structures through the application of weak magnetic fields with little to no field gradient.[30–32] These weak uniform fields lead to the alignment of the magnetic particles as opposed to particle migration and agglomeration toward the surface, which created structures that were stronger in an additional orthogonal direction as opposed to only the ice-templating direction. To achieve these weak uniform fields, a Helmholtz coils setup was utilized.[30–32,35,36] Helmholtz coils are a pair of symmetric electromagnets that are spaced such that the separation distance between them is equal to the radius of both coils. When spaced at such a distance, the coils are then able to apply a nearly uniform field at the center point between them and, therefore, throughout the freeze-casting setup.[37] If one wants to apply multiple fields simultaneously, pairs of coils can be arranged orthogonally to one another while still maintaining their field uniformity throughout the setup. A ubiquitous configuration of multiple coils is the bi-axial Helmholtz coils setup, which consists of two sets of coils arranged orthogonally from one another. This setup allows the user to apply weak uniform magnetic fields in multiple directions simultaneously. This setup has allowed the user to apply complex field types during the freeze-casting process, such as rotating,[35] diagonal,[30] bouligand,[35] and oscillating fields.[32,36] All these complex field types allowed for complex control over the freeze-cast structure. The application of oscillating fields, in particular, during the freeze-casting process has been shown to increase both the mechanical strength and microstructural control of ferrimagnetic (e.g., iron oxide) freeze-cast materials[32] as well as non-ferrimagnetic (e.g., titania) freeze-cast materials.[36] This control over non-ferrimagnetic materials was achieved through a combination of oscillating fields as well as the surface magnetization process.

While much research has been done over applying magnetic fields to freeze-cast structures with either weak and uniform fields or strong and non-uniform fields, little to no research has been done comparing these fields to one another through applying them to similar freeze-cast materials. To this end, this research will focus on applying weak, uniform magnetic fields produced from a bi-axial Helmholtz coils setup to ferrimagnetic iron oxide and comparing it to similar materials fabricated under strong, non-uniform magnetic fields produced by a permanent magnet setup. Two fields of similar magnitudes were applied to the freeze-cast structures, one produced by the Helmholtz coils setup, and one produced by the permanent magnet setup, and compared to one another. Then, each setup had an optimized field applied to the freeze-cast structures and then compared to one another; the optimized field for the Helmholtz coils was an oscillating field, and for the permanent magnet setup, it was a field with a very large magnitude. After comparison, these results could better illustrate the benefits of weak, uniform fields,
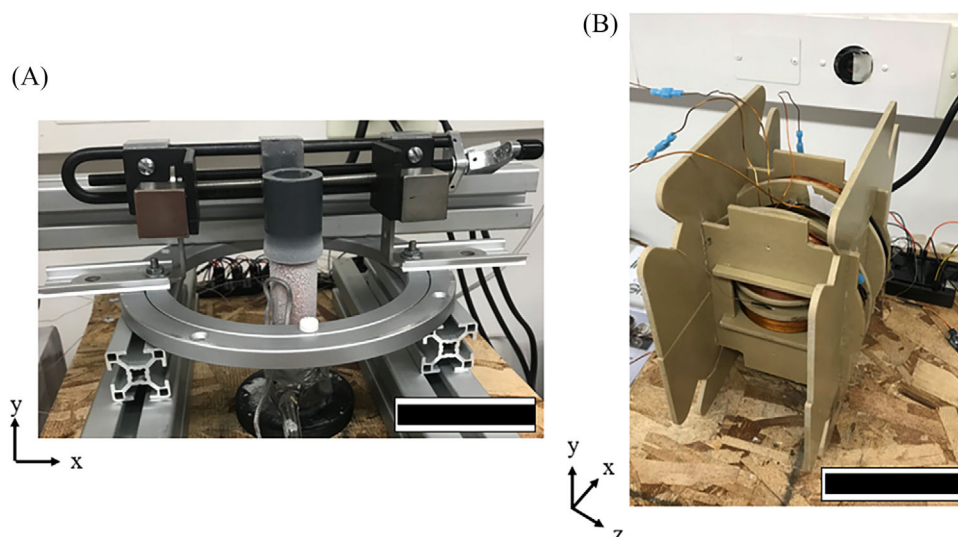
FIGURE 1 (A) View of the permanent magnet setup used to apply the strong and non-uniform magnetic, and the coordinate system used with it. The *x*-direction corresponds to the applied field direction, and the *y*-direction corresponds to the ice-growth direction. (B) Trimetric view of the bi-axial Helmholtz coils used in this study along with the coordinate system utilized. The large coils correspond to the *x*-direction or applied field direction, and the small coils correspond with the *y*-direction or ice-growth direction. Both scale bars correspond to 10 cm.

in particular uniform fields produced by Helmholtz coils setups and could potentially be applied to a wider range of material types, in particular more bio-compatible materials, thus increasing the applications of these tailored, porous materials.[36]

2 | MATERIALS AND METHODS

2.1 | Non-uniform magnetic field generation

To produce non-uniform magnetic fields for this study, a permanent magnet setup was fabricated. The setup, inspired by Frank et al.,[27] consisted of a self-centering vice centered over a circular turnstile. The turnstile allows the user to easily change the orientation of the permanent magnets, while the self-centering vise allows the user to change the separation distance between the permanent magnets, which dictates the magnetic field strength. Two neodymium cubic permanent magnets, both 1 in³ in size and N50 grade, were placed on either side of the self-centering vise and then placed over the freeze-casting setup, similar to the Helmholtz coils setup, to generate these strong, non-uniform magnetic fields (see Figure 1A). To verify that the correct magnitude was being applied, the magnets were brought to a specific separation distance, and then the magnitude was measured using an Adafruit TLV493 magnetometer and compared to the following

equation derived from the charge model:

$$\vec{b} = \frac{\mu_0 \, Q_{\mathrm{m}}}{4\pi S} \frac{\left(\vec{x} - \vec{x}'\right)}{\left|\vec{x} - \vec{x}'\right|^3}$$

where $\vec{b}$ is the magnetic field at a point in space, Q_{m} is the surface charge of the magnet, S is the magnetic shielding factor, $\vec{x}$ is the vector to the point of interest, and $\vec{x}'$ is the vector to the surface charge. This was repeated multiple times to verify the correct magnitude being applied at various separation distances.

2.2 | Uniform magnetic field generation

To produce weak, uniform magnetic fields, a bi-axial Helmholtz coils setup was used (see Figure 1B). These coils were utilized and manufactured in a previous study.[36] In this previous study, they were tested and shown to provide accurate magnetic fields with negligible field gradients, resulting in nearly uniform, or uniform magnetic fields, comparable to previous studies.[31] The coils were controlled via computer using LabVIEW software, allowing the user to specify the magnitude, direction, or frequency of the field in multiple orthogonal directions, including the ice-templating or *y*-direction and the *x*-direction or applied field direction.
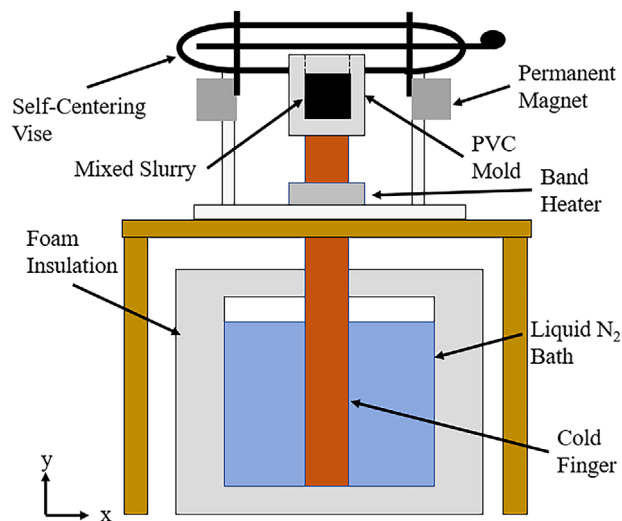
FIGURE 2 Detailed diagram of the freeze-casting setup used to fabricate all the scaffolds for this study. The permanent magnet setup is pictured over the freeze-casting setup for application of the strong, non-uniform fields. The Helmholtz coils setup was placed similarly over the setup for the application of the weak, uniform fields.

2.3 | Sample preparation

Iron oxide II/III from ACROS Organics was used as the solid loading compound in the freeze-cast slurries. The slurry consisted of the solid loading compound at 10 vol%, the binder polyvinyl alcohol at 1 wt% and polyethylene glycol at 1 wt%, the additive octanol at 0.435 wt% as an anti-foaming agent, and the particle dispersant Darvan 811 at 1 wt%. Each slurry was 11 mL in total volume. Once measured, each slurry was mixed on a vortex mixer for 2 min and degassed in a dome under vacuum for 5 min. Once degassed, the slurries were immediately poured into a Polyvinyl Chloride mold atop a copper cold finger submerged in a bath of N_2 in a custom freeze-casting setup (see Figure 2), as used in previous experiments.[32,36] A thermocouple and band heater were attached to the cold finger to both monitor the temperature as well as decrease it at a constant rate of 10°C/min. All slurries were directionally frozen in the vertical or y-direction. A total of 25 scaffolds were fabricated. The scaffolds were fabricated under one of the following field types:

- No field (NF): no field was applied during the freeze-casting process.
- Constant field (CF): a uniform field was applied from a bi-axial Helmholtz coils setup in the x-direction at a constant magnitude of 20 mT.
- Permanent low field (PLF): a non-uniform field was applied from a permanent magnet setup in the x-direction at a constant magnitude of 20 mT.

- 30% oscillation (30%): a uniform field was applied from a bi-axial Helmholtz coils setup in the x-direction at a constant magnitude of 20 mT, along with an alternating field in the y-direction ranging between 6 mT and −6 mT at 5 rpm.
- Permanent high field (PHF): a non-uniform field was applied from a permanent magnet setup in the x-direction at a constant magnitude of 40 mT.

Five scaffolds were fabricated under each field type. In all cases, the field type was applied throughout the entire freezing process. After freezing the slurries, they were lyophilized at 0.02 Torr at −65°C in a Labconco Free Zone 1 freeze drier for 72 h to sublimate all the ice crystals from the scaffolds, resulting in green bodies. Once lyophilized, the green bodies were placed in an open-air Keith KSK-12 1700 furnace and were sintered at 1125°C for 20 min, with a heating and cooling rate of 3°C/min, resulting in solid scaffolds that could then be mechanically tested and their microstructure analyzed.

2.4 | Permanent high-field scaffolds

Preliminary scaffolds were freeze-cast under various magnitudes of the PHF to determine the maximum field strength that could be applied from the PHF while still producing a porous scaffold. One scaffold was fabricated under the field strengths of 75, 50, 40, and 30 mT. A section from the middle of each scaffold was then cut and removed and images of the porosity were taken using a scanning electron microscope (SEM, FEI Quanta 600 FG). The percent porosity of the scaffold was then analyzed using the ImageJ software, and the percent porosity was then compared to a freeze-cast scaffold fabricated under a weak, uniform field to determine if it was still a porous structure. Once the chosen field strength was determined, its scaffold profile on the x–z and y–z faces was imaged, and the major and minor axes on the x–z face was measured to determine its eccentricity and this was compared to the profile on the x–z and y–z faces of a scaffold fabricated under the 30% as well as a scaffold fabricated under NF to determine how much the strong, non-uniform field distorted the freeze-cast scaffold.

2.5 | Mechanical testing

The densified scaffolds were mechanically tested on an Instron 5967 load frame with an Instron 30 kN load cell. The scaffolds were prepared for mechanical testing by cutting eight cubes from the midsection of each scaffold with a diamond saw. Four of the cubes were compressed normal
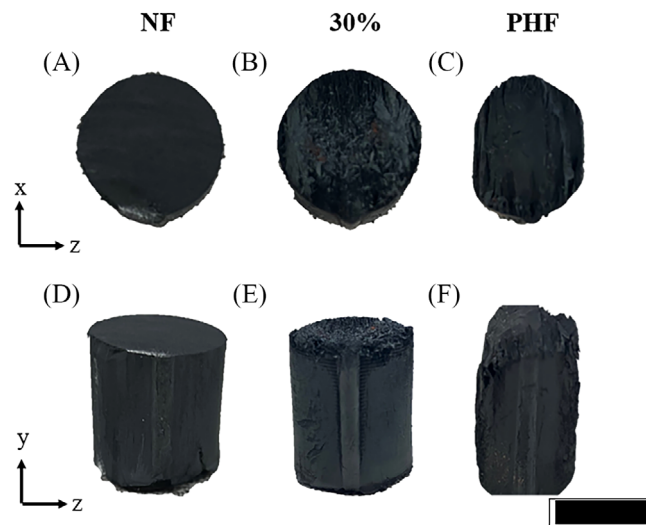
FIGURE 3 (A–C) Image of the *x–z* face of scaffolds under the field types: no field (NF), 30% oscillation (30%), and permanent high field (PHF). The NF scaffold represents the control scaffold and the other two scaffolds had their eccentricity compared to it to determine how much each applied field type distorted the physical structure. (D–F) Image of the *y–z* face of the same scaffolds. The scale bar corresponds to 15 mm.

to the *y*-direction or ice-growth direction, and four cubes were compressed normal to the *x*-direction or the direction of the applied constant magnetic field for each scaffold based on field type. Each cube had an average height of 5 mm and an average area of 25 mm^2. All were compressed at a crosshead speed of 1 mm/min. The ultimate compression strength (UCS) and modulus of elasticity (*E*) were recorded during each test, with the UCS being recorded as the highest engineering compression stress and the *E* being recorded as the slope of the linear-elastic region of the stress–strain curve. A total of 20 compression tests were completed in each of the *x*-direction and *y*-direction for all five different field types.

2.6 | Material characterization

To characterize and view the microstructure of the densified scaffolds, images were taken of the scaffolds for each field type using a SEM. The imaging of each scaffold was taken on material sectioned from the center of the scaffold. All images were taken on the in-plane or *x–z* face. A total of 20 scaffolds were imaged, five for each of the different field types. Once taken, the images were analyzed using the ImageJ photo analysis software. This software allows the user to identify many different features of the microstructure, including the wall thickness, average area porosity, pore area, pore major axis length, and pore minor axis size. The measurements for wall thickness were made at

500× magnification and the rest of the measurements were made at 200× magnification. The results of these were the mean of 400 measurements for five scaffolds for each of the NF, CF, PLF, 30%, and PHF for the wall thickness analysis, and the mean of 2000 measurements from five scaffolds for the average area porosity, average pore size, and size of the major and minor axes. The wall thickness, major axis, and minor axis were all recorded in units of micrometers (μm), the average pore size was recorded in units of micrometers squared (μm^2), and the area porosity was recorded in a unitless percentage (%).

The alignment of the lamellar walls was also analyzed using the ImageJ software to determine how the wall alignment was affected by the five different applied field types. The images were analyzed along the *x–z* face. Using a previously published process,[30,32,36] wall alignment was measured and binned into four separate sectors ($-45° \pm 22.5°$, $-0° \pm 22.5°$, $45° \pm 22.5°$, $90° \pm 22.5°$) to determine the relative directionality of the walls.

2.7 | Statistical analysis

A statistical analysis was performed on the mechanical and microstructural data of the scaffolds using a one-way ANOVA test in MATLAB software. The five different field types were considered: NF, CF, PLF, 30%, and PHF. The field types were divided into two groups and compared to only different field types in that same group. The two groups were first: NF, CF, and PLF, and then NF, 30%, and PHF. Each test was run using a standard significant of $\alpha = 0.05$; if the test reported a *p*-value less than the α value stated above, then the tested data were considered statistically significant. If statistical significance was identified, a Tukey's honest significant difference test was then run on the data to view the significance of individual pairwise comparisons, to see which specific field type was significant from another.

3 | RESULTS AND DISCUSSION

3.1 | Permanent high-field strength

After imaging the *x–z* face of each preliminary scaffold as well as the reference scaffold and analyzing their percent porosity, it was seen that the percent porosity seemed to plateau after applying 40 mT and was comparable to the reference porosity (see Figure S1). Therefore. The field strength of 40 mT was chosen as the magnitude of the PHF, as this was the highest observed field strength that still produced a porous structure.

As shown in Figure 3, the profiles of the PHF scaffold fabricated under 40 mT as well as one fabricated under
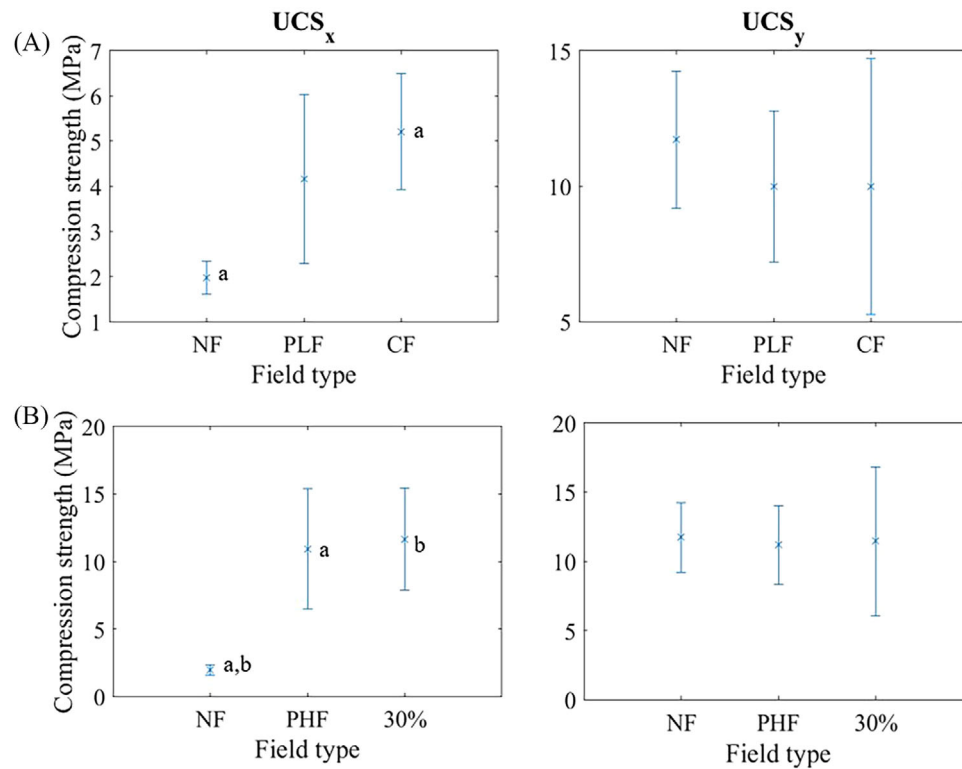
FIGURE 4 Mean compression strength as a function of field types: (A) no field (NF), permanent low field (PLF), and constant field (CF), and (B) NF, permanent high field (PHF), and 30% oscillation (30%) in both the x-direction or applied field direction and y-direction or ice-templating direction. Data presented are the mean of $n = 20$ measurements and the error bars represent $\pm$ one standard deviation. Pairs of means that have statistically significant differences are labeled by the same lower-case letter.

30% and a scaffold fabricated under NF can be seen. When NF was applied, the $x–z$ profile was measured to have an eccentricity of 1.00, being essentially a perfect circle. This can be verified by looking at Figure 3A,D, as both profiles seem to be circular and cylindrical, respectively. When the 30% field was applied, the $x–z$ profile was measured to have an eccentricity of 1.01, once again being essentially a perfect circle. This can once again be verified by looking at Figure 3B,E, as both profiles seem to be circular and cylindrical, respectively. Last, when a strong, non-uniform field was applied, the $x–z$ profile was measured to have an eccentricity of 1.40 signifying an elongated ellipse as opposed to a circular shape. Looking at both Figure 3C,F, this can be verified as the $x–z$ profile is much more elongated in the x direction, as well as looking at the $y–z$ profile where the structure looks almost rectangular, thus signifying that the application of the strong, non-uniform field led to significant distortion of the physical structure.

3.2 | Mechanical results

As shown in Figure 4A, the UCS can be seen as a function of field types NF, CF, and PLF for both the x-direction (UCS$_x$, applied field direction) as well as the y-direction (UCS$_y$, ice-growth direction). The CF led to the highest UCS$_x$, while NF led to the lowest UCS$_x$. The CF was significant from NF, with a p-value = 4E-3. Looking at UCS$_y$, all field types had roughly the same strength, with no field types significant from one another. Therefore, it can be concluded that the CF was able to strengthen the freeze-cast structure in the x-direction or applied field direction, while the PLF was unable.

The UCS as a function of the field types NF, 30%, and PLF for the x-direction (UCS$_x$, applied field direction) as well as the y-direction (UCS$_y$, ice-growth direction) is shown in Figure 4B. Once again, NF led to the lowest UCS$_x$, while 30% led to the strongest UCS$_x$. Both 30% and PHF were very significant from NF, with both p-values $\leq$9.4E-16. Considering the UCS$_y$, once again all field types had similar compression strengths, with no significance between any of the field types. In addition, the compressive strengths in the x- and y-directions were about the same strength for both the 30% and PHF scaffolds, with no statistically significant distances between the x- and y-compressive strengths for both field types, thus signifying a transversely isotropic structure in the x- and y-directions from these field types.
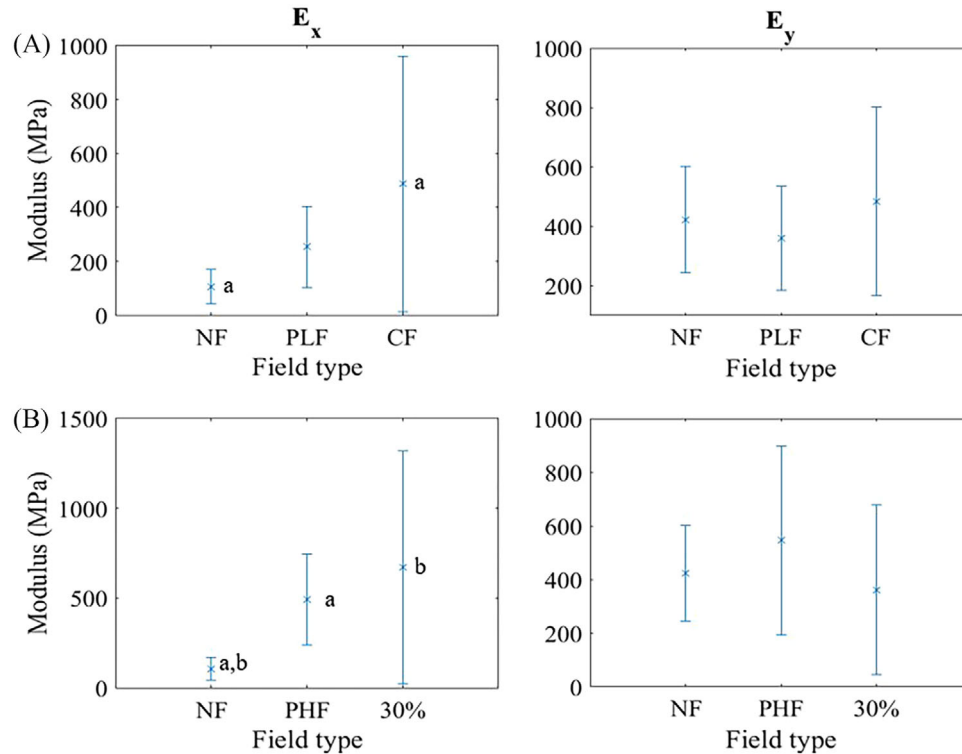
FIGURE 5 Mean modulus of elasticity as a function of field types: (A) no field (NF), permanent low field (PLF), and constant field (CF), and (B) NF, permanent high field (PHF), and 30% oscillation (30%) in both the *x*-direction or applied field direction and *y*-direction or ice-templating direction. Data presented are the mean of $n = 20$ measurements and the error bars represent $\pm$ one standard deviation. Pairs of means that have statistically significant differences are labeled by the same lower-case letter.
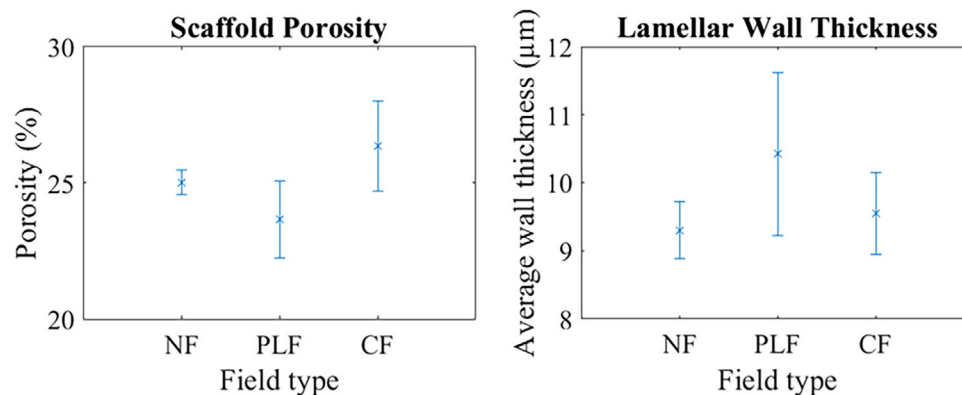

FIGURE 6 Mean scaffold percent porosity and lamellar wall thickness as a function of field types: no field (NF), permanent low field (PLF), and constant field (CF). Data presented are the mean of $n = 10$ measurements and the error bars represent $\pm$ one standard deviation. Pairs of means that have statistically significant differences are labeled by the same lower-case letter.

E_x and E_y for the field types NF, CF, and PLF can be seen in Figure 5A. The CF led to the highest E_x or most stiff structures, while NF led to the lowest E_x. The CF was also statistically significant from the NF with a *p*-value = 1.9E-2. Looking at E_y, all field types reported similar moduli, with no statistical significance between the field types.

As shown in Figure 5B, E_x and E_y for the field types NF, 30%, and PHF can be seen. Once again, the NF led to the lowest E_x, while 30% led to the highest or stiffest structure. In addition, both the 30% and PHF were significant from NF, with both *p*-values $\leq$1.7E-2. All fields reported similar moduli for E_y once again, with no statistical significance found between any field types.
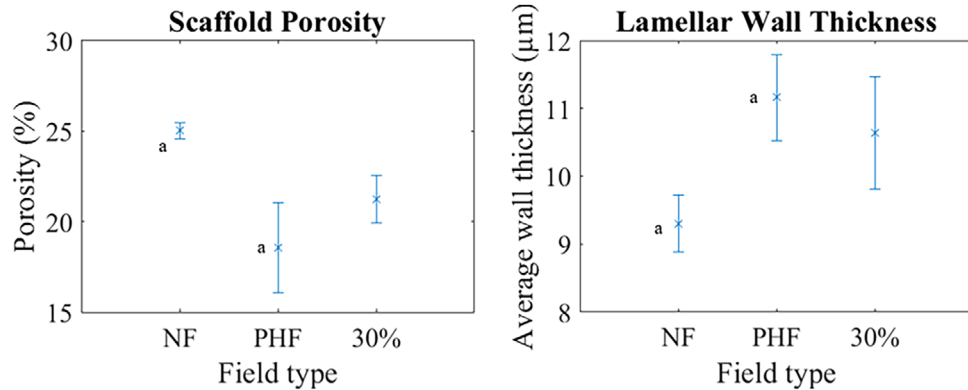
FIGURE 7 Mean scaffold percent porosity and lamellar wall thickness as a function of field types: no field (NF), permanent high field (PHF), and 30% oscillation (30%). Data presented are the mean of $n = 10$ measurements and the error bars represent ± one standard deviation. Pairs of means that have statistically significant differences are labeled by the same lower-case letter.

Comparing these results to previous experiments, it was shown in previous studies that applying a constant uniform field as well as an oscillating field led to stronger structures in the x-direction or applied field direction when compared to when NF was applied.[30,32] The results agree with this, as it was shown that the 30% and CF led to increases in UCS_x when compared to NF. It has also been shown in previous research that application of a strong, non-uniform field has led to increases in UCS_x in the x-direction when compared to when NF was applied, which also agrees with these results.[27] In addition, no degradation or weakening was found in the y-direction or ice-growth direction when the 30% or CF was applied, which also agrees with past studies.[30,32] In addition, while error bars of a larger magnitude were reported for the USC and E, looking at previous freeze-casting research, comparable degrees of error can be seen in the mechanical data,[29,38,39] thus signifying that the degrees of error reported were not unusual or of concern. Last, it has been shown in previous studies that the application of both weak and uniform fields as well as strong and non-uniform fields has led to increases in the modulus or stiffness of the scaffolds when compared to when NF is applied.[30] This also agrees with these results, as it was shown that the CF, 30%, and PHF all led to stiffer structures when compared to when NF was applied.

Comparing the results of the weak and uniform fields from the Helmholtz coils to the strong and non-uniform fields from the permanent magnet setup, it was seen that when both fields applied the same magnitude, the CF led to an increase in mechanical strength in the x-direction compared to when NF was applied, while the PLF did not. When both field types were optimized, the 30% and PHF both led to significant increases in mechanical strength in the x-direction compared to when NF was applied and similar strengths overall. Essentially, at the same mag-

nitude, the uniform field produced superior mechanical results compared to the non-uniform field, while at half the magnitude the weak, uniform field produced similar mechanical results to the strong, non-uniform field. Therefore, it can be determined that weak, uniform fields produce superior mechanical results compared to strong, non-uniform fields.

3.3 | Microstructural results

The microstructure of the freeze-cast scaffolds was also analyzed to determine how the microstructure was controlled based on the factor of applied field type. Figures 6 and 7 show the average lamellar wall thickness and percent porosity for the field types NF, CF, PLF and NF, 30%, PHF, respectively. The NF, CF, and PLF all had similar average lamellar wall thickness and percent porosity, with no statistical significance between any of these three field types. The PHF however, had both the lowest percent porosity as well as the largest average lamellar wall thickness. It was statistically significant from NF in terms of both percent porosity and lamellar wall thickness with both p-values ≤2.6E-2. This lower porosity for the PHF scaffolds when compared to the NF scaffolds is most likely a contributing factor for increased mechanical strength, as it has been shown previously that decreased porosity leads to increases in mechanical strength in freeze-cast scaffolds.[36]

As shown in Table 1, additional microstructural data can be seen, including the average pore size, the major and minor axis lengths, and the eccentricity of the pores, all as a function of field type. The 30% had the largest average pore size while NF had the smallest, 30% had the largest major and minor axes, NF had the smallest major axis, PHF had the smallest minor axis, and PHF

TABLE 1 The microstructural properties as a function of all field types, including the average pore area, average major axis, average minor axis, and average eccentricity of the pores.

Magnetic field type	Pore area (μm^2)	Major axis (μm)	Minor axis (μm)	Eccentricity
NF	133 ± 19.7	18.3 ± 1.33^b	7.70 ± 0.35	2.37 ± 0.15
CF	199 ± 32.4	23.5 ± 3.23	8.40 ± 0.97	2.81 ± 0.43
PLF	158 ± 36.4	20.7 ± 2.74	7.73 ± 0.59	2.68 ± 0.32
30%	205 ± 50.0^a	24.1 ± 4.19^b	8.76 ± 0.74^c	2.76 ± 0.51
PHF	120 ± 48.4^a	19.0 ± 3.77	6.54 ± 1.49^c	2.95 ± 0.30

Note: All data are reported as the mean $\pm$ one standard deviation of 2000 measurements for $n = 5$ scaffolds for each field type. Comparisons that have statistically significant differences ($\alpha = 0.05$) are labeled by the same lower-case letter (a–c).

Abbreviations: CF, constant field; NF, no field; PHF, permanent high field; PLF, permanent low field; 30%, 30% oscillation.

had the largest eccentricity, with NF having the lowest eccentricity. Therefore, even though the 30% had a very large average pore area compared to NF, its pores tended to be less circular and more elongated due to its higher eccentricity, while NF had many more circular pores, leading to longer and thinner channels between walls.

It was shown that the 30% and PHF scaffolds were the strongest overall in the x-direction. Further investigation of the microstructure can be performed to explain this increase in mechanical strength. This investigation was performed by analyzing the alignment of the lamellar walls on the x–z face. Directionality plots of the lamellar wall alignment as well as SEM images of the lamellar walls on the x–z face for each field type can be seen in Figures 8 and 9 for all field types. Looking at Figure 8A, when NF is applied, there is no directionality or control over the walls. This can be verified by looking at Figure 8d, where a general randomness of the lamellar walls can be observed and there seems to be no directionality, as is expected given the random growth of ice.[30,32] In Figure 8B, when the PLF was applied, some alignment in the applied field or x-direction can be seen, with about half of the lamellar walls aligning in the x-direction. Verifying this with Figure 8E, a decent amount of the lamellar walls point in the x-direction. Last, Figure 8C shows that when the CF was applied, a large majority of lamellar walls were pointing in the applied field or x-direction, about two-thirds of all the walls. This can once again be verified by looking at Figure 8F, where a majority of the lamellar walls are pointing in the x-direction. Considering the NF, PHF, and 30% in Figure 9, in Figure 9B when the PHF is applied, a similar percentage of walls to the CF are aligned in the applied field direction. Figure 9E verifies this, as a large amount of the lamellar walls are aligned in the applied field direction. The best alignment can be seen in Figure 9C when the 30% is applied. Nearly every lamellar wall is aligned in

the applied field direction, with over 98% alignment. Seeing Figure 9F verifies this, as every wall is aligned in the applied field direction.

The alignment of these lamellar walls is most likely what led to the increase in mechanical strength for the CF, PHF, and 30%, as previous research has shown that alignment of the microstructure has led to increases in mechanical strength.[30,32] When comparing the CF scaffolds to the PLF scaffolds, it is interesting to note that even though both fields applied the same magnitude, the CF led to more alignment in the x-direction. This would make sense as the mechanical strength of the CF was significant from the NF scaffolds, while the PLF scaffolds were not. Comparing the 30% scaffolds to the PHF scaffolds, the 30% led to much higher alignment, even with only half of the field strength of the PHF. This increased alignment from the 30% compared to PHF makes sense, as they had similar mechanical strengths, but the PHF also had a lower percent porosity, being significant from NF while the 30% was not. Therefore, the higher field strength of the PHF combined with decreased porosity as well as lamellar wall alignment produced comparable mechanical strength that the 30% was able to achieve through a lower field strength and wall alignment alone. Another critical note about the alignment achieved through the 30% is that while previous research has shown that application of magnetic fields, in particular weak uniform magnetic fields, has led to increased lamellar wall alignment, little to no research has shown the degree of control over the microstructure that the 30% achieved with essentially all walls aligned in the direction of the applied magnetic field. Application of non-uniform fields has led to only 60% alignment,[14] while application of a uniform, CF has led to about 75% alignment,[30] which is still significantly lower than the complete control achieved through the oscillating field.

These results show that first, when comparing uniform fields produced by a Helmholtz coils setup to non-uniform fields produced by a permanent magnet setup, at similar magnitudes the Helmholtz coils produced superior mechanical results while also leading to greater control over the microstructure, in particular as shown from the alignment of the lamellar walls when compared to the permanent magnet setup. When optimizing for both setups, applying an oscillating field for the Helmholtz coils setup and a high field magnitude for the permanent magnet setup, it was shown that both setups led to similar increases in mechanical strength compared to when NF was applied, in addition to leading to a transversely isotropic material in the x- and y-directions. Both setups also increased the stiffness of the scaffolds compared to when NF was applied. The permanent magnet setup led to a decrease in porosity, with the Helmholtz coils setup
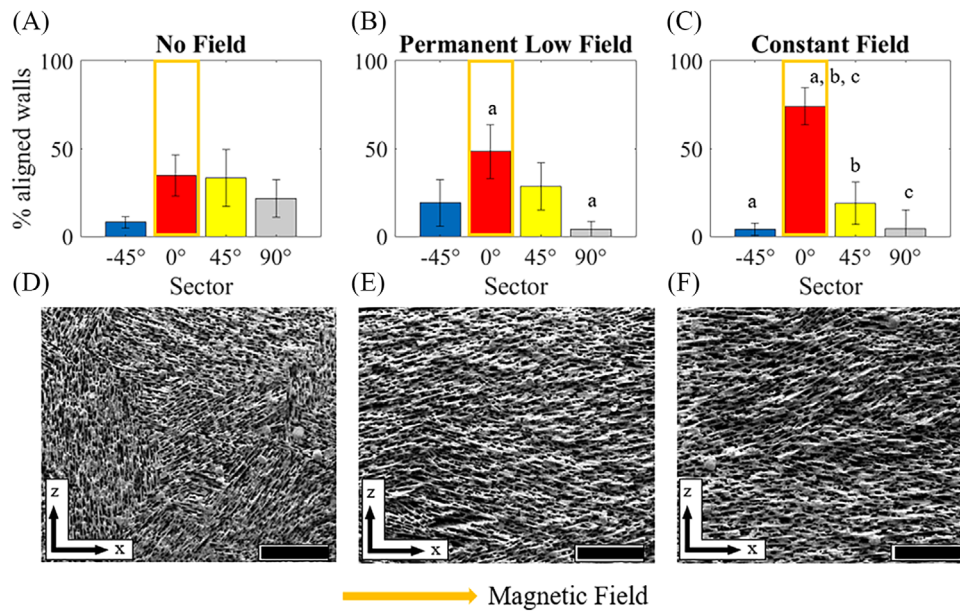
FIGURE 8 Percent of walls that align within four different sectors: $-45° \pm 22.5°$, $-0° \pm 22.5°$, $45° \pm 22.5°$, and $90° \pm 22.5°$. The x-direction corresponds to $0°$ and the z-direction corresponds to $90°$. Plots of lamellar wall alignment and scanning electron microscopy (SEM) images along the x–z plane for (A and D) no field, (B and E) permanent low field, and (C and F) constant field. Data presented are the mean value obtained from $n = 5$ scaffolds per field type, and the error bars represent $\pm$ one standard deviation. All scale bars correspond to 200 μm.
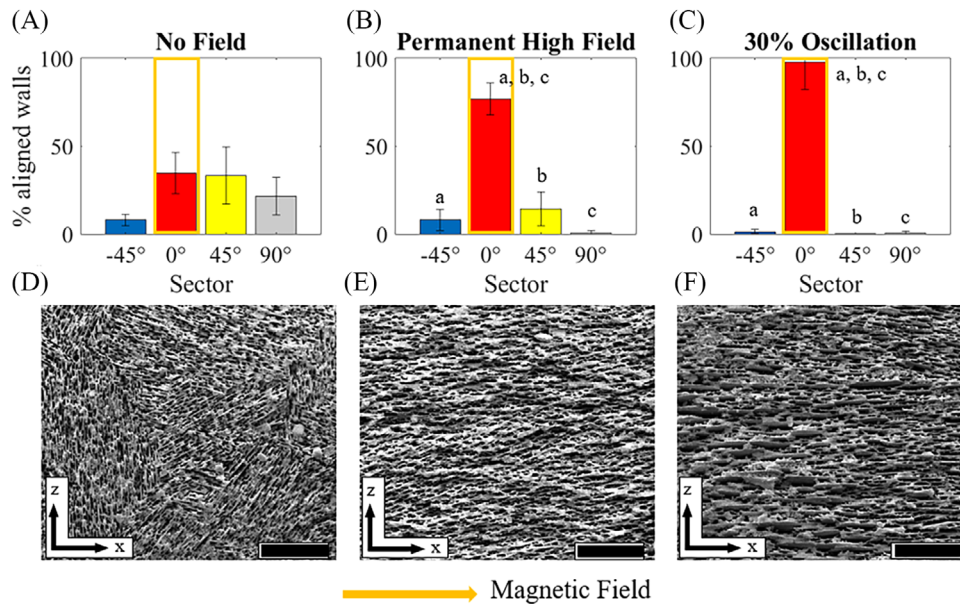

FIGURE 9 Percent of walls that align within four different sectors: $-45° \pm 22.5°$, $-0° \pm 22.5°$, $45° \pm 22.5°$, and $90° \pm 22.5°$. The x-direction corresponds to $0°$ and the z-direction corresponds to $90°$. Plots of lamellar wall alignment and scanning electron microscopy (SEM) images along the x–z plane for (A and D) no field, (B and E) permanent high field, and (C and F) 30% oscillation. Data presented are the mean value obtained from $n = 5$ scaffolds per field type, and the error bars represent $\pm$ one standard deviation. All scale bars correspond to 200 μm.

maintaining scaffold porosity and leading to complete control over the lamellar wall alignment. Therefore, it can be stated that the Helmholtz coils setup led to superior results when compared to the permanent magnet setup, as at similar magnitudes the Helmholtz coils setup led to superior mechanical and microstructural results, while at half the magnitude, the Helmholtz coils led to similar mechanical results in addition to superior microstructural control. In addition, it can be stated that the structure–property relationship of the freeze-cast

scaffolds was impacted by magnetic freeze casting, particularly Helmholtz coil-assisted freeze casting. Application of these uniform fields produced by the Helmholtz coils setup could led to freeze-cast scaffolds with optimized mechanical properties as well as complete microstructural control.

4 | CONCLUSIONS

Based on this study of comparing weak and uniform fields produced by a Helmholtz coils setup to strong and non-uniform fields produced by a permanent magnet setup, the following conclusions can be drawn:

1. The application of a uniform field of the same magnitude as a non-uniform field leads to superior mechanical results in the applied field, or x-direction, for iron-oxide freeze-cast structures.
2. The application of a uniform field of the same magnitude as a non-uniform field leads to superior control of the microstructure through the alignment of lamellar walls for iron-oxide freeze-cast structures.
3. The application of an oscillating field to iron-oxide freeze-cast structures leads to similar mechanical strength in the applied field, or x-direction, compared to a much larger non-uniform field produced by a permanent magnet setup.
4. The microstructure of iron-oxide freeze-cast structures, in particular the alignment of the lamellar walls, can be completely controlled through the application of an oscillating field.
5. The Helmholtz coils setup leads to superior mechanical and microstructural results when compared to a permanent magnet setup for iron-oxide freeze-cast structures.

ORCID
Josh R. Fernquist https://orcid.org/0000-0002-7943-288X

REFERENCES
1. Hammel EC, Ighodaro OL-R, Okoli OI. Processing and properties of advanced porous ceramics: an application based review. Ceram Int. 2014;40(10):15351–70. https://doi.org/10.1016/j.ceramint.2014.06.095
2. Deville S, Saiz E, Tomsia AP. Freeze casting of hydroxyapatite scaffolds for bone tissue engineering. Biomaterials. 2006;27(32):5480–89. https://doi.org/10.1016/j.biomaterials.2006.06.028
3. Tang Y, Zhao K, Hu L, Wu Z. Two-step freeze casting fabrication of hydroxyapatite porous scaffolds with bionic bone graded structure. Ceram Int. 2013;39(8):9703–7. https://doi.org/10.1016/j.ceramint.2013.04.038
4. Lee E-J, Koh Y-H, Yoon B-H, Kim H-E, Kim H-W. Highly porous hydroxyapatite bioceramics with interconnected pore channels using camphene-based freeze casting. Mater Lett. 2007;61(11):2270–73. https://doi.org/10.1016/j.matlet.2006.08.065
5. Wei G, Ma PX. Structure and properties of nano-hydroxyapatite/polymer composite scaffolds for bone tissue engineering. Biomaterials. 2004;25(19):4749–57. https://doi.org/10.1016/j.biomaterials.2003.12.005
6. Kang H-W, Tabata Y, Ikada Y. Fabrication of porous gelatin scaffolds for tissue engineering. Biomaterials. 1999;20(14):1339–44. https://doi.org/10.1016/S0142-9612(99)00036-8
7. Largeot C, Portet C, Chmiola J, Taberna P-L, Gogotsi Y, Simon P. Relation between the ion size and pore size for an electric double-layer capacitor. J Am Chem Soc. 2008;130(9):2730–31. https://doi.org/10.1021/ja7106178
8. Schoof H, Apel J, Heschel I, Rau G. Control of pore structure and size in freeze-dried collagen sponges. J Biomed Mater Res. 2001;58(4):352–57. https://doi.org/10.1002/jbm.1028
9. Sofie SW, Dogan F. Freeze casting of aqueous alumina slurries with glycerol. J Am Ceram Soc. 2001;84(7):1459–64. https://doi.org/10.1111/j.1151-2916.2001.tb00860.x
10. Sofie SW. Fabrication of functionally graded and aligned porosity in thin ceramic substrates with the novel freeze-tape-casting process. J Am Ceram Soc. 2007;90(7):2024–31. https://doi.org/10.1111/j.1551-2916.2007.01720.x
11. Araki K Halloran JW. Porous ceramic bodies with interconnected pore channels by a novel freeze casting technique. J Am Ceram Soc. 2005;88(5):1108–14. https://doi.org/10.1111/j.1551-2916.2005.00176.x
12. Naleway SE, Fickas KC, Maker YN, Meyers MA, McKittrick J. Reproducibility of ZrO_2-based freeze casting for biomaterials. Mater Sci Eng C. 2016;61:105–12. https://doi.org/10.1016/j.msec.2015.12.012
13. Qian L, Zhang H. Controlled freezing and freeze drying: a versatile route for porous and micro-/nano-structured materials. J Chem Technol Biotechnol. 2011;86(2):172–84. https://doi.org/10.1002/jctb.2495
14. Frank MB, Siu SH, Karandikar K, Liu C-H, Naleway SE, Porter MM, et al. Synergistic structures from magnetic freeze casting with surface magnetized alumina particles and platelets. J Mech Behav Biomed Mater. 2017;76:153–63. https://doi.org/10.1016/j.jmbbm.2017.06.002
15. Hunger PM, Donius AE, Wegst UGK. Platelets self-assemble into porous nacre during freeze casting. J Mech Behav Biomed Mater. 2013;19:87–93. https://doi.org/10.1016/j.jmbbm.2012.10.013
16. Deville S, Maire E, Lasalle A, Bogner A, Gauthier C, Leloup J, et al. In situ X-ray radiography and tomography observations of the solidification of aqueous alumina particle suspensions—part I: initial instants. J Am Ceram Soc. 2009;92(11):2489–96. https://doi.org/10.1111/j.1551-2916.2009.03163.x

17. Deville S, Maire E, Bernard-Granger G, Lasalle A, Bogner A, Gauthier C, et al. Metastable and unstable cellular solidification of colloidal suspensions. Nat Mater. 2009;8(12):966–72. https://doi.org/10.1038/nmat2571

18. Hunger PM, Donius AE, Wegst UGK. Structure–property-processing correlations in freeze-cast composite scaffolds. Acta Biomater. 2013;9(5):6338–48. https://doi.org/10.1016/j.actbio.2013.01.012

19. Preiss A, Su B, Collins S, Simpson D. Tailored graded pore structure in zirconia toughened alumina ceramics using double-side cooling freeze casting. J Eur Ceram Soc. 2012;32(8):1575–83. https://doi.org/10.1016/j.jeurceramsoc.2011.12.031

20. Bai H, Chen Y, Delattre B, Tomsia AP, Ritchie RO. Bioinspired large-scale aligned porous materials assembled with dual temperature gradients. Sci Adv. 2015;1(11). https://doi.org/10.1126/sciadv.1500849

21. Bai H, Walsh F, Gludovatz B, Delattre B, Huang C, Chen Y, et al. Bioinspired hydroxyapatite/poly(methyl methacrylate) composite with a nacre-mimetic architecture by a bidirectional freezing method. Adv Mater. 2016;28(1):50–56. https://doi.org/10.1002/adma.201504313

22. Bai H, Wang D, Delattre B, Gao W, De Coninck J, Li S, et al. Biomimetic gradient scaffold from ice-templating for self-seeding of cells with capillary effect. Acta Biomater. 2015;20:113–19. https://doi.org/10.1016/j.actbio.2015.04.007

23. Moon J-W, Hwang H-J, Awano M, Maeda K. Preparation of NiO–YSZ tubular support with radially aligned pore channels. Mater Lett. 2003;57(8):1428–34. https://doi.org/10.1016/S0167-577X(02)01002-9

24. Tang Y, Miao Q, Qiu S, Zhao K, Hu L. Novel freeze-casting fabrication of aligned lamellar porous alumina with a centrosymmetric structure. J Eur Ceram Soc. 2014;34(15):4077–82. https://doi.org/10.1016/j.jeurceramsoc.2014.05.040

25. Tang Y, Qiu S, Miao Q, Wu C. Fabrication of lamellar porous alumina with axisymmetric structure by directional solidification with applied electric and magnetic fields. J Eur Ceram Soc. 2016;36(5):1233–40. https://doi.org/10.1016/j.jeurceramsoc.2015.12.012

26. Ogden TA. Bioinspired ultrasound freeze casting: engineered porous scaffolds through freeze casting and ultrasound directed self-assembly [online]. M.S. Thesis. UT, USA: The University of Utah; 2019. Available from: https://www.proquest.com/docview/2496206030/abstract/4F4366FD0D0E4001PQ/1 Accessed 25 Aug 2021

27. Frank MB, Naleway SE, Haroush T, Liu C-H, Siu SH, Ng J, et al. Stiff, porous scaffolds from magnetized alumina particles aligned by magnetic freeze casting. Mater Sci Eng C. 2017;77:484–92. https://doi.org/10.1016/j.msec.2017.03.246

28. Porter MM, Meraz L, Calderon A, Choi H, Chouhan A, Wang L, et al. Torsional properties of helix-reinforced composites fabricated by magnetic freeze casting. Compos Struct. 2015;119:174–84. https://doi.org/10.1016/j.compstruct.2014.08.033

29. Porter MM, Niksiar P, McKittrick J. Microstructural control of colloidal-based ceramics by directional solidification under weak magnetic fields. J Am Ceram Soc. 2016;99(6):1917–26. https://doi.org/10.1111/jace.14183

30. Nelson I, Gardner L, Carlson K, Naleway SE. Freeze casting of iron oxide subject to a tri-axial nested Helmholtz-coils driven uniform magnetic field for tailored porous scaffolds. Acta Mater. 2019;173:106–16. https://doi.org/10.1016/j.actamat.2019.05.003

31. Nelson I, Ogden TA, Al Khateeb S, Graser J, Sparks TD, Abbott JJ, et al. Freeze-casting of surface-magnetized iron(II,III) oxide particles in a uniform static magnetic field generated by a Helmholtz coil. Adv Eng Mater. 2019;21(3):1801092. https://doi.org/10.1002/adem.201801092

32. Fernquist JR, Fu HC, Naleway SE. Improved structural and mechanical performance of iron oxide scaffolds freeze cast under oscillating magnetic fields. Ceram Int. 2022;48(11):15034–42. https://doi.org/10.1016/j.ceramint.2022.02.032

33. Nelson I, Naleway SE. Intrinsic and extrinsic control of freeze casting. J Mater Res Technol. 2019;8(2):2372–85. https://doi.org/10.1016/j.jmrt.2018.11.011

34. Porter MM, Yeh M, Strawson J, Goehring T, Lujan S, Siripasopsotorn P, et al. Magnetic freeze casting inspired by nature. Mater Sci Eng A. 2012;556:741–50. https://doi.org/10.1016/j.msea.2012.07.058

35. Nelson I, Varga J, Wadsworth P, Mroz M, Kruzic JJ, Kingstedt OT, et al. Helical and bouligand porous scaffolds fabricated by dynamic low strength magnetic field freeze casting. JOM. 2020;72(4):1498–508. https://doi.org/10.1007/s11837-019-04002-9

36. Fernquist JR, Nelson I, Pourkand A, Abbott JJ, Naleway SE. Improved strength and control over surface-magnetized titania porous structures freeze cast under oscillating magnetic fields. Materialia. 2023;32:101905. https://doi.org/10.1016/j.mtla.2023.101905

37. Abbott JJ. Parametric design of tri-axial nested Helmholtz coils. Rev Sci Instrum. 2015;86(5):054701. https://doi.org/10.1063/1.4919400

38. Silva AMA, Nunes EHM, Souza DF, Martens DL, da Costa JCD, Houmard M, et al. Effect of titania addition on the properties of freeze-cast alumina samples. Ceram Int. 2015;41(9):10467–75. https://doi.org/10.1016/j.ceramint.2015.04.132

39. Nezafati N, Hafezi M, Zamanian A, Naserirad M. Effect of adding nano-titanium dioxide on the microstructure, mechanical properties and in vitro bioactivity of a freeze cast merwinite scaffold. Biotechnol Prog. 2015;31(2):550–56. https://doi.org/10.1002/btpr.2042

SUPPORTING INFORMATION

Additional supporting information can be found online in the Supporting Information section at the end of this article.